JARS Journal of Applied Remote Sensing

RESEARCH PAPER

Robustness of gross primary production estimation from long-term reconstructed solar-induced chlorophyll fluorescence varies with greenness on a global scale

Lijiang Fu,[a] Qian Xia,[a,b] Hao Tang,[a] Junqing Chen,[c] Jinglu Tan,[c] and Ya Guo[a,*]
[a]Jiangnan University, Ministry of Education, Key Laboratory of Advanced Process Control for Light Industry, Wuxi, China
[b]Changshu Institute of Technology, School of Electrical Engineering and Automation, Changshu, China
[c]University of Missouri, Department of Chemical and Biomedical Engineering, Columbia, Missouri, United States

ABSTRACT. Long-term reconstructed solar-induced chlorophyll fluorescence (SIF) derived from raw gridded SIF has been used for the estimation of gross primary production (GPP), but the robustness of the spatial relationship may vary from location to location. We examined the often-used linear relationship between GPP and SIF in terms of R^2 values for varied locations globally using three GPP datasets (FLUXCOM, VPM, PML) and three long-term reconstructed monthly SIF datasets (CSIF, SIF005, and RTSIF). The results show that the R^2 value is a concave function of vegetation greenness level (NDVI) on an annual or seasonal basis. The average R^2 is over 0.8 in areas where the annual average NDVI is in the range of 0.4 to 0.6, whereas the R^2 is much lower where the annual average NDVI is less than 0.2 or greater than 0.8. Prediction of GPP or SIF by three methods from five major environmental variables revealed greater uncertainties in GPP and/or SIF at low or high greenness levels as an apparent cause of the low R^2. The results offer useful insights into how global GPP may be effectively estimated from multi-satellite measured SIF.

[DOI: 10.1117/1.JRS.19.014514]

Keywords: gross primary production estimation; long-term reconstructed solar-induced fluorescence; correlation analysis

Paper 240558G received Sep. 16, 2024; revised Jan. 7, 2025; accepted Jan. 17, 2025; published Feb. 5, 2025.

1 Introduction

Gross primary production (GPP), as the largest component of the global carbon cycle, drives the functioning of global ecosystems.[1,2] With the increase in extreme climate events, accurate estimation of GPP can provide useful information for understanding and managing the ecological environment. GPP exhibits strong spatiotemporal heterogeneity because of different vegetation types, phenology, and meteorological conditions.[3,4] The Fluxnet network, consisting of more than 200 eddy covariance measurement sites of different landcovers and climate types, synthesizes GPP-related data as the basis for quantifying terrestrial photosynthesis around the world. Limited spatial and temporal data resolutions, however, hinder the widespread use of global GPP estimates from the network because an individual flux site only measures CO_2 fluxes over ~1 km^2.[5,6]

---

*Address all correspondence to Ya Guo, guoy@jiangnan.edu.cn

Handling Editor: Qian Du, Editor-in-Chief

Various models have been used for the estimation of global GPP, and the models can be largely classified into three types:[2] (1) data-based models—these models are mainly based on data analysis by machine learning and other methods to derive relationships between CO_2 flux observations and optical indices or climate variables. Examples include FLUXCOM GPP[7] and MTE GPP.[8] The accuracy of data-based models often depends on the density of regional sites.[6] For areas with few measurement sites, the estimation accuracy of GPP is generally low; (2) light use efficiency (LUE) models—LUE models are mainly based on empirical equations of light energy utilization in photosynthesis. The main differences between various LUE models are in the environmental stress factors or the maximum LUE factor used.[2] MODIS GPP[9] and VPM GPP[10] are LUE models. The limitations of these models lie in the *a priori* $\mathrm{LUE}_{\mathrm{max}}$ and the limited roles of the selected stress factors; (3) process-based models—these models are based on the physiological processes of vegetations, which include PML GPP[11] and BESS GPP.[12] The complexity of plant physiological processes in different areas and meteorological conditions leads to a diversity of model parameters and the need for input information, which in turn leads to uncertainties in GPP estimation.[13,14] In general, a simple model structure cannot track regional productivity dynamics, especially in extreme environmental conditions or low-productivity regions, while complex model structures, especially process-based models, may involve uncertainties and propagation of uncertainties from input data.[13]

Solar-induced fluorescence (SIF), a co-product of plant photosynthesis, is sensitive to plant physiological changes.[15,16] With the retrievals of satellite-based SIF data such as Greenhouse Gases Observing Satellite (GOSAT), Scanning Imaging Absorption Spectrometer for Atmospheric Chartography (SCIAMACHY), Global Ozone Monitoring Experiment-2 (GOME-2), and Orbiting Carbon Observatory-2 (OCO-2), Tropospheric Monitoring Instrument (TROPOMI); SIF-based ecosystem environmental stresses monitoring[17] and photosynthetic capacity inversions[18,19] have become the latest research efforts. SIF has shown potential for estimating GPP from specific sites to global spatial scales[20–22] or from instantaneous to monthly time scales[23–26] because of its good linear relationships with GPP. Raw SIF datasets, however, are rough patterns of the global SIF distribution obtained by averaging noisy, sparse, and infrequent samples over large footprint sizes.[27] For long-term and high-resolution needs, long-term reconstructed SIF datasets based on fusion methods and other remote sensing data (such as surface reflectance) are generated, which include CSIF,[28] SIF005,[29] GOSIF,[30] RSIF,[31] and RTSIF.[32] As a result of their long-time spans and high spatial resolutions, they are widely used in the estimation of regional or global GPP.[33,34] Shekhar et al. showed the advantages of four reconstructed SIF datasets over NDVI (normalized difference vegetable indices) and EVI (enhanced vegetable indices) in estimating GPP of different vegetation types at the site scales.[35] NDVI, nonetheless, is a greenness index widely used to indicate differences in vegetation density and health.

On a global scale, the signal-to-noise ratio of remote-sensing data, vegetation phenology, physiological or physical factors, viewing-illumination geometry, and environmental factors collectively and interactively affect the relationship between GPP and SIF, but the intrinsic mechanisms underpinning such cross-scale relationships are still unknown.[36] As a result, although a spatial distribution of the ratio of GPP over SIF can result in a fine-grained estimation of GPP based on SIF, the reliability of such a linear relationship between GPP and SIF may vary with location and needs to be examined. Chen et al. presented a global distribution of the GPP/SIF ratio in a normalized form, showing that the GPP/SIF spatial distributions in tropical rainforest and Australian shrublands areas vary with the selected GPP or SIF datasets.[37] An analysis of the robustness of GPP estimation from SIF globally based on different data sources may help reduce biases introduced by the processing of GPP and SIF data, but such studies are lacking. Vegetation greenness, often measured with NDVI, represents vegetation growth state and coverage.[38] It is, therefore, meaningful to analyze the dependence of the relationship between GPP and SIF on greenness levels.

Environmental variables are important factors affecting ecosystem functions and therefore the GPP–SIF relationship.[39] Environmental variables are widely used as inputs for predicting regional or global GPP and SIF based on different machine learning methods.[7,28,30] Variations in the influences of environmental variables on GPP and SIF will change the consistency of variations between the two and thus add uncertainties in the GPP–SIF relationship.

Determining the environmental effects on GPP and SIF is thus helpful in explaining the changes in GPP–SIF relationship in different regions.

In this work, we analyzed the robustness of the linear relationship between GPP and SIF on a global scale based on three commonly used GPP datasets and three long-term reconstructed SIF datasets. This entailed (1) evaluating GPP variations globally to illustrate their dependence on greenness (NDVI), (2) assessing the robustness of GPP prediction from long-term reconstructed SIF as influenced by greenness, and (3) analyzing possible sources of variability by observing the influences of environmental variables on GPP and SIF in different greenness levels based on machine learning methods.

2 Materials and Methods

2.1 GPP Data

Three GPP datasets, the FLUXCOM GPP (a data-based model), the PML GPP (a process-based model), and the VPM GPP (an LUE model) were used. The FLUXCOM GPP data were derived from training three machine learning algorithms (model tree ensemble, artificial neural networks, and multivariate adaptive regression splines and random forests) based on data from 224 FLUXNET sites, meteorological measurements, and satellite data.[7,40] All FLUXCOM GPP data are available from Ref. 41. Average monthly data from 2001 to 2018 resampled to a spatial resolution of 0.5 deg were used for this study.

The PML GPP dataset is produced from a coupled diagnostic biophysical model,[11] which was originally derived from a biophysical model for surface conductance (G_s) based on the Penman–Monteith (PM) equation.[42] Monthly PML GPP data with a spatial resolution of 0.5 deg from 2003 to 2017 are processed by the Google Earth Engine.[43]

The VPM GPP dataset is based on the LUE model, and it is expressed as the product of maximum light energy use efficiency ($\varepsilon_{\max}$), photosynthetic active radiation (PAR) absorbed by chlorophylls (APAR), temperature stress limitation (T_{scalar}), and water stress limitation (W_{scalar}):

$$\text{GPP} = \varepsilon_{\max} \times T_{\text{scalar}} \times W_{\text{scalar}} \times \text{APAR}, \tag{1}$$

where APAR is expressed as the product of the fraction of absorbed photosynthetic active radiation by chlorophylls (fPAR) and PAR with fPAR estimated from EVI, T_{scalar} and W_{scalar} in are expressed as follows, respectively:[10,44]

$$T_{\text{scalar}} = \frac{(T - T_{\max}) \times (T - T_{\min})}{(T - T_{\max}) \times (T - T_{\min}) - (T - T_{\text{opt}})^2}, \tag{2}$$

$$W_{\text{scalar}} = \frac{1 + \text{LSWI}}{1 + \text{LSWI}_{\max}}, \tag{3}$$

where $T_{\min}$, $T_{\max}$, and T_{opt} are the minimum, maximum, and optimum temperatures for vegetation photosynthesis, respectively; $\text{LSWI}_{\max}$ is the maximum LSWI (land surface water index) during the growing season over several years; ε_0 is a biome-specific parameter and is obtained from a lookup-table (LUT) from the MODIS land cover data. Monthly data with a spatial resolution of 0.5 deg from 2001 to 2016 are from Ref. 45.

2.2 SIF Data

Three long-term and high-resolution SIF datasets generated by fusion methods (e.g., machine learning), named CSIF,[28] SIF005,[29] and RTSIF,[32] were used in this study. CSIF was produced by training a neural network with surface reflectance from MODIS and daily sounding-based SIF retrievals at 757 nm from OCO-2. Data at 0.5 deg spatial resolution and 4-day temporal resolution, available from Ref. 46, were averaged to monthly resolution from 2001 to 2016 in this work.

SIF005 was based on a framework that circumvents the discrepancies, such as retrievals, instrument characteristics, overpass time, and viewing-illumination angles, based on cumulative distribution function (CDF) matching to correct the offset between SIF values between SCIAMACHY and GOME-2. Monthly data at 0.05 deg spatial resolution are available from

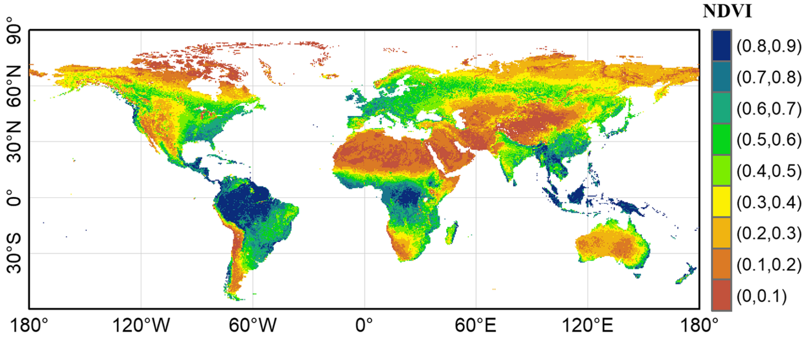

Fig. 1 Annual average NDVI from 2001 to 2020.

Ref. 47. They were resampled to 0.5 deg spatial resolution from 2003 to 2018 without changes to the time interval.

RTSIF is produced by running the Extreme Gradient Boosting (XGBoost) algorithm on raw un-gridded TROPOMI SIF data, surface reflectance, PAR, land surface temperature, land cover, and C3/C4 fraction. Data at 0.05 deg spatial and 8-day temporal resolutions, available from Ref. 48, were resampled to 0.5 deg spatial resolution and monthly time interval from 2001 to 2020.

2.3 Vegetation Greenness

The annual NDVI data from the MODIS satellite were used to represent vegetation greenness.[1] Monthly NDVI values at 0.05 deg spatial resolution are directly available from MOD13C2.[49] They were resampled to 0.5 deg spatial resolution in this work. Figure 1 shows the global annual average NDVI divided into nine levels from 0 to 1. The global average NDVI values for the four seasons (MAM: March to May, JJA: June to August, SON: September to November, DJF: December to February) were also calculated (Fig. 11 in Appendix).

2.4 Landcover

The dominant land cover class from MCD12C1 is used in this study,[49] of which adopt the International Geosphere–Biosphere Program (IGBP) land cover classification scheme consisting of 17 major land cover classes.[50] In this study, eight major vegetation classes were used, which include CRO (croplands), DBF (deciduous broadleaf forest), EBF (evergreen broadleaf forest), ENF (evergreen needles forest), GRA (grasslands), MF (mixed forest), SAV (savannas and woody savannas), and SHR (closed shrublands and open shrublands). To match the GPP and SIF data, land cover data were aggregated to 0.5 deg-by-0.5 deg grids by the nearest sampling method. An example global distribution of the eight major vegetation types is shown in Fig. 12 in the Appendix.

2.5 Climate Data

Environmental variables, including SWR (short-wavelength radiation), minimum temperature (TMP), precipitation (PRE), vapor pressure deficit (VPD), and soil moisture (SM), from TerraClimate were used in this work. TerraClimate is a dataset with monthly climate and climatic water balance for global terrestrial surfaces. It uses climatically aided interpolation with high-spatial-resolution climatological normals from the WorldClim dataset and coarser-spatial-resolution and time-varying data from CRU Ts4.0 and the Japanese 55-year Reanalysis (JRA55).[51] Monthly climate data with a spatial resolution of 0.5 deg from 2001 to 2020 are processed in this work using the Google Earth Engine.[52]

2.6 Data Analysis

On a global scale, the linear relationship between GPP and SIF provides a direct and effective method for estimating global GPP based on readily available SIF data.[33,34] It is thus meaningful to analyze the robustness of this linear dependence in terms of R^2 values from different data sources of GPP and SIF. Linear regression of GPP versus SIF was performed for each location (pixel). The resulting slope and R^2 as functions of location and greenness level.

Partial least squares regression (PLSR), random forests (RF), and K-nearest neighbor (KNN) algorithms with five inputs and two outputs were used to determine the effects of environmental variables, including short-wavelength radiation (SWR), minimum temperature (TMP), precipitation (PRE), vapor pressure deficit (VPD), and soil moisture (SM), on GPP and SIF. In this study, the prediction of GPP or SIF based on environmental variables was implemented at each location (pixel). Compared with other machine learning algorithms and deep learning algorithms, PLSR, RF, and KNN are more efficient and suitable for small-scale data sets and have low parameter adjustment complexity. For model training, 80% of monthly data for each location (pixel) were randomly selected and the remaining 20% were used for model testing. The R^2 values for GPP and SIF prediction were determined for each pixel and then analyzed as functions of location and greenness level.

3 Results

3.1 Global GPP Variations with Season and Greenness

To observe GPP variations globally, the seasonal averages of the three GPP datasets are displayed in Fig. 2. The datasets show similar seasonal patterns on the global scale. In MAM (March to May), the high-GPP areas are mainly in the tropical rain forests, southwestern United States, East Asia, and Europe. In JJA (June to August), the high-GPP areas are mainly in the tropical rain forests, Western United States, and Eurasia except for Central Asia. In SON (September to November), the high-GPP areas are mainly in the tropical rain forests, whereas in DJF (December to February), the high-GPP areas are mainly in southern Africa and South America.

The GPP maps in Fig. 2 show a positive correlation between vegetation greenness and GPP yield, as can be expected, which is confirmed by the plot of GPP versus NDVI in Fig. 3. Among the three datasets, PML gives higher GPP than FLUXCOM and VPM where NDVI > 0.2. Compared with FLUXCOM, VPM GPP gives higher GPP at lower greenness levels but lower GPP at higher greenness levels. In addition, the temporal GPP correlations among the three datasets show similar global patterns and are the lowest ($R^2 < 0.5$) in the EBF areas in the rainforest and the SHR areas in Australia (Fig. 4), which shows greater inconsistencies and uncertainties in

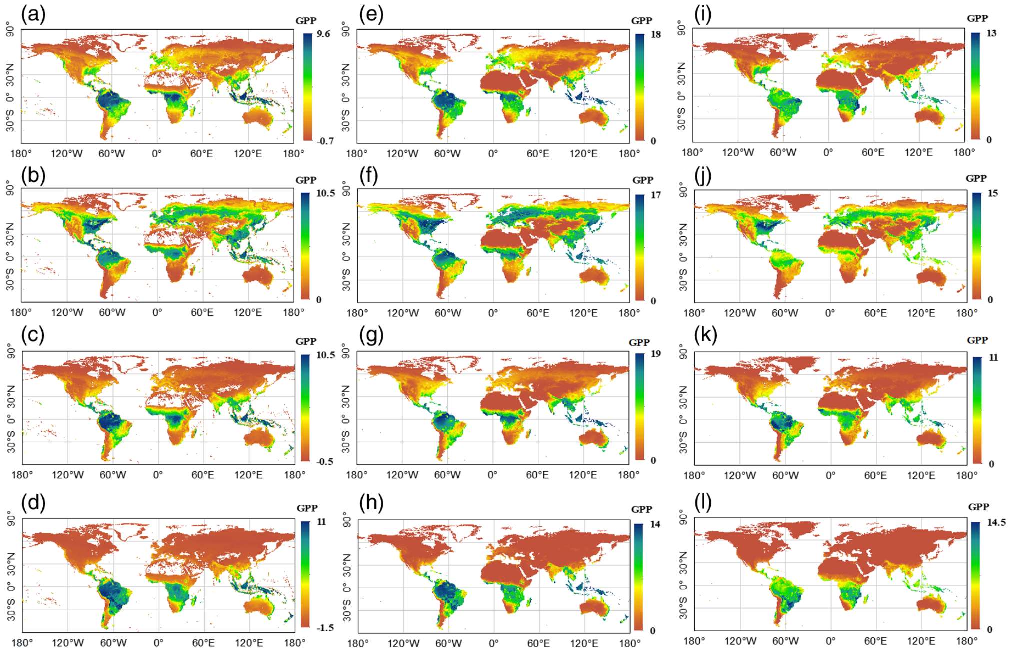

Fig. 2 Spatial patterns of seasonal mean values of the three GPP datasets. MAM (March to May), JJA (June to August), SON (September to November), and DJF (December to February). (a) FLUXCOM_MAM. (b) FLUXCOM_JJA. (c) FLUXCOM_SON. (d) FLUXCOM_DJF. (e) PML_MAM. (f) PML_JJA. (g) PML_SON. (h) PML_DJF. (i) VPM_MAM. (j) VPM_JJA. (k) VPM_SON. (l) VPM_DJF.

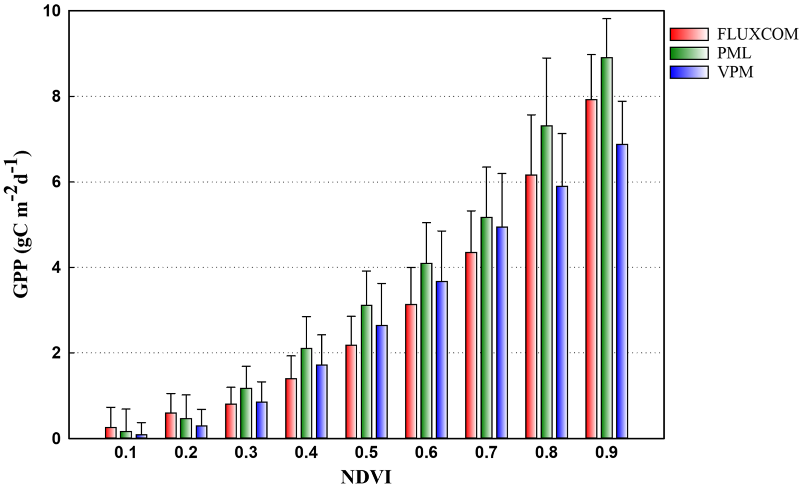

Fig. 3 Variations of GPP with greenness levels.

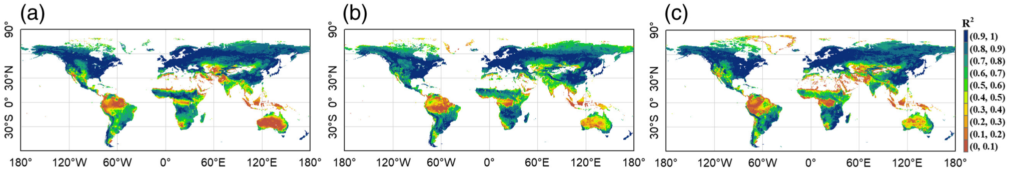

Fig. 4 Linear correlations between GPP datasets. (a) FLUXCOM versus PML. (b) FLUXCOM versus VPM. (c) PML versus VPM.

estimating GPP in these regions. The strong dependence of GPP on greenness indicates that the dependence of GPP on SIF may also vary with greenness as shown in the following subsection.

3.2 Global Variations in the Linear Dependence of GPP on SIF

Linear regression was used to analyze the dependence of GPP on SIF for different locations and Fig. 5 shows the spatial distribution of the regression R^2 values for each of the three GPP datasets

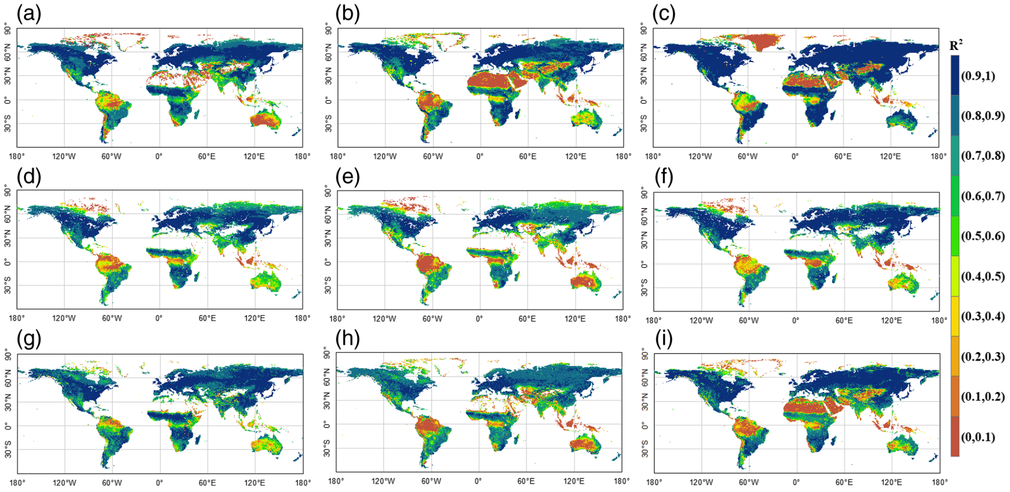

Fig. 5 Spatial patterns of R^2 for linear regression of each of the three GPP datasets versus each of the three SIF datasets. The timeframe for each pair was determined by the intersection of the GPP and SIF datasets: (a) FLUXCOM versus CSIF: 2001 to 2016; (b) PML versus CSIF: 2003 to 2016; (c) VPM versus CSIF: 2001 to 2016; (d) FLUXCOM versus SIF005: 2003 to 2018; (e) PML versus SIF005: 2003 to 2017; (f) VPM versus SIF005: 2003 to 2016; (g) FLUXCOM versus RTSIF: 2001 to 2018; (h) PML versus RTSIF: 2003 to 2017; (i) VPM versus RTSIF: 2001 to 2016.

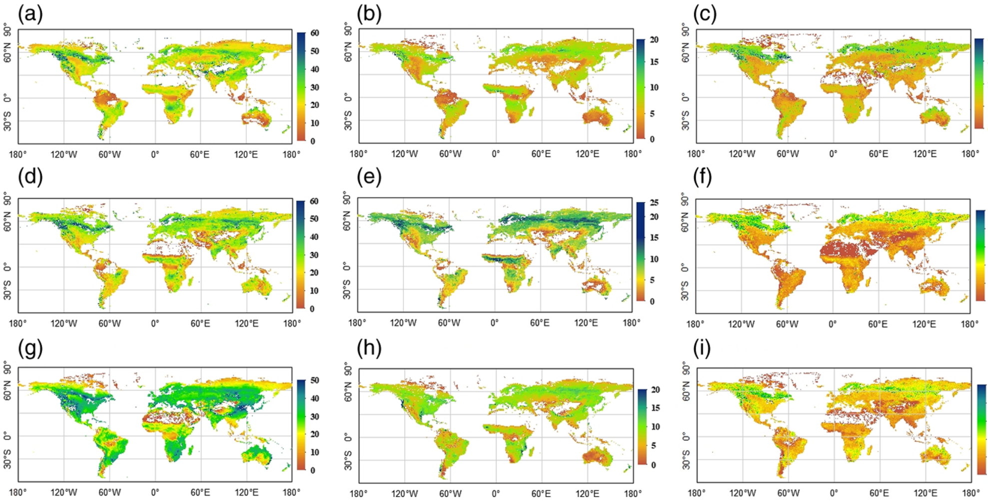

Fig. 6 Spatial patterns of slopes of linear regression between each of the three GPP datasets and each of the three SIF datasets. The GPP–SIF data pairs are indicated by the subfigure labels. (a) FLUXCOM versus CSIF; (b) FLUXCOM versus SIF005; (c) FLUXCOM versus RTSIF; (d) PML versus CSIF; (e) PML versus SIF005; (f) VPM versus SIF005; (g) FLUXCOM versus RTSIF; (h) PML versus RTSIF; (i) VPM versus RTSIF.

(FLUXCOM, PML, VPM) with respect to each of the three long-term reconstructed SIF datasets (CSIF, SIF005, RTSIF). The results show generally high correlations between SIF and GPP, especially in areas above 30° N, but the R^2 values vary greatly with location. In particular, the R^2 is low for Central Asia, North Africa, the tropical rainforest, and Australian shrublands.

For further analysis of the spatial variations in the regression R^2, the slope values of linear regression of GPP versus SIF are mapped in Fig. 6 for different pairs of GPP and SIF datasets. The regression slope values depend on the data pair as shown by the differences among the subfigures, but an interesting observation can be made from the relative variations within each subfigure. For areas with relatively high R^2 in Fig. 2, such as areas above 30° N, the slope values are relatively high and uniform, while for areas with relatively low R^2, such as Central Asia and the tropical rainforest, the slope values tend to be low, variable, or both. A low slope value indicates a weak dependence of GPP on SIF, whereas slope variations indicate a lack of consistency, both of which lead to low R^2 values.

Comparing Fig. 1 with Figs. 2 and 4 reveals a form of association between greenness and regression R^2 and slope (examine Central Asia, North Africa, the tropical rainforest, and Australia, where the NDVI is low or high). Figure 7 plots the R^2 against the annual average NDVI values (binned into nine discrete levels) for different GPP and SIF dataset combinations. The linear regression R^2 values of GPP versus SIF show a strong dependence on the greenness

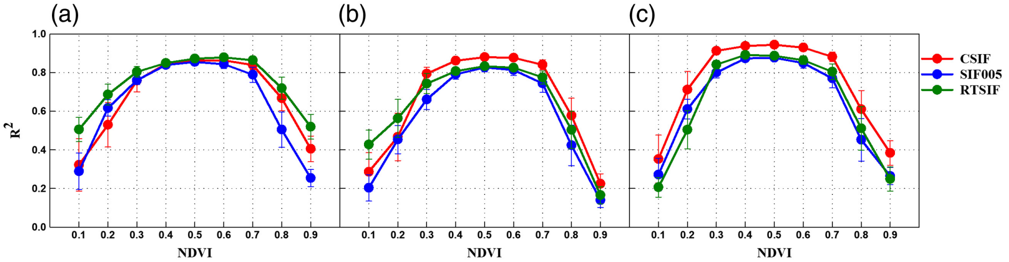

Fig. 7 Linear regression R^2 of GPP versus SIF for different dataset combinations as a function of greenness level. The NDVI values were rounded up to the nearest tenth; thus, 0.1 represents the interval [0, 0.1], and 0.2 represents the interval (0.1, 0.2] and so on. (a) FLUXCOM. (b) PML. (c) VPM.

level for all the dataset pairs. With increasing greenness level, the regression R^2 increases first, levels, and then decreases as a concave function of NDVI. The R^2 reaches a maximum (average R^2 over 0.8) in areas where the annual average NDVI is in the range of 0.4 to 0.6. The R^2 is much lower where the annual average NDVI is less than 0.2 or greater than 0.8.

For further analysis of its dependence on greenness, linear regression of GPP versus SIF was performed by season and the R^2 is plotted in Fig. 8 against the average NDVI for the four seasons (shown in Fig. 11 in Appendix). The linear regression R^2 of GPP versus SIF remains a concave function of greenness level for all seasons and dataset pairs. The R^2 in the MAM and SON seasons is higher than that in JJA and DJF across the NDVI levels. In MAM and SON, the R^2 in the mid-level NDVI areas can be higher than 0.8, but the highest R^2 in JJA and DJF is only about 0.6, except for the VPM-CSIF dataset pair in JJA (Fig. 8).

Since different greenness levels often result from different vegetations, linear regression of GPP versus SIF was performed by vegetation classes and the R^2 values are plotted with respect to the annual average NDVI in Fig. 9. The results show that while different vegetation classes appear in different ranges of NDVI, the regression R^2 curves collectively make up a concave function similar to the overall R^2 values shown in Fig. 7. The low-greenness areas with low R^2 are mainly GRA and SHR vegetation classes, whereas high-greenness areas with low R^2 are mainly EBF and SAV vegetation classes. Some vegetation classes such as GRA and SAV are widely distributed around the world, and their NDVI levels and R^2 vary greatly in different areas. Other vegetation classes, such as CRO, DBF, ENF, and MF, are mainly in the middle levels of greenness with high R^2.

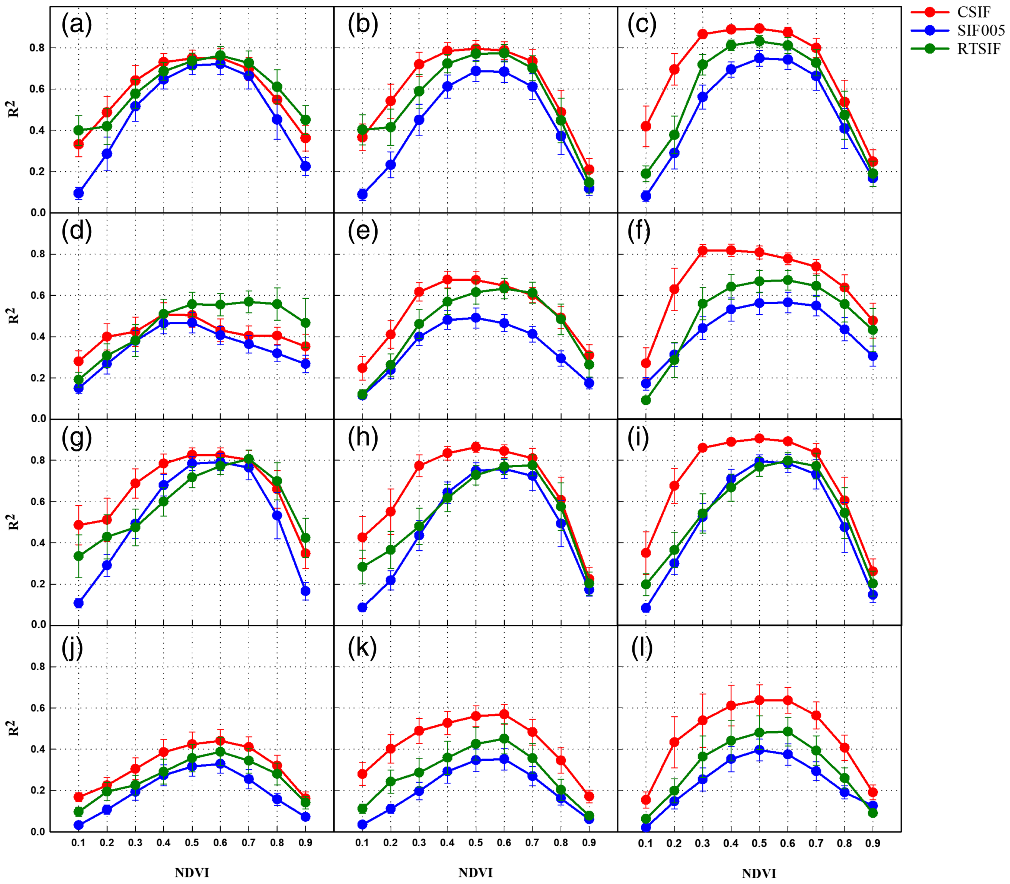

Fig. 8 Linear regression R^2 of GPP versus SIF by season as a function of greenness level for different dataset combinations (MAM: March to May, JJA: June to August, SON: September to November, DJF: December to February). (a) MAM_FLUXCOM; (b) MAM_PML; (c) FLUXCOM versus RTSIF; (d) PML versus CSIF; (e) PML versus SIF005; (f) PML versus RTSIF; (g) VPM versus CSIF; (h) VPM versus SIF005; (i) VPM versus RTSIF.

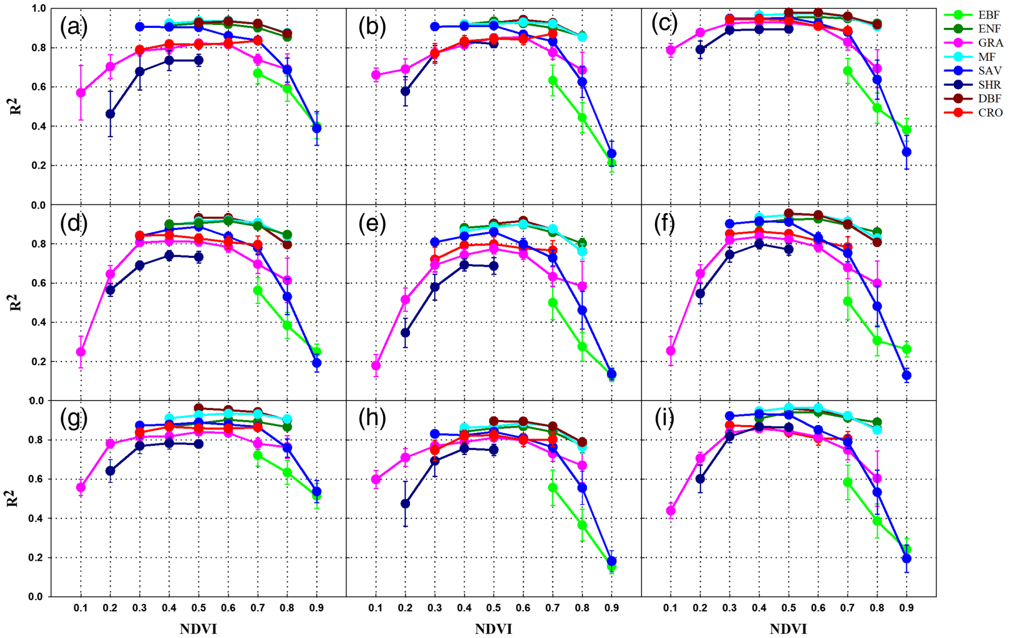

Fig. 9 Regression R^2 of GPP versus SIF by vegetation classes for nine combinations of GPP and SIF datasets as functions of greenness levels. CRO—croplands, DBF—deciduous broadleaf forest, EBF—evergreen broadleaf forest, ENF—evergreen needles forest, GRA—grasslands, MF—mixed forest, SAV—savannas and woody savannas, and SHR—closed shrublands and open shrublands. (a) FLUXCOM versus CSIF; (b) PML versus CSIF; (c) VPM versus CSIF; (d) FLUXCOM versus SIF005; (e) PML versus SIF005; (f) VPM versus SIF005; (g) FLUXCOM versus RTSIF; (h) PML versus RTSIF; (i) VPM versus RTSIF.

3.3 Influence of Environmental Variables on GPP and SIF

As an analysis of possible sources of variation in the GPP–SIF relationship, the influences of five commonly used environmental variables on GPP and SIF were observed by training models with five inputs (SWR, TMP, PRE, VPD, and SM) and two outputs (GPP, SIF) by three methods. The GPP and SIF prediction R^2 values for the tested datasets are plotted in Fig. 10 as functions of NVDI for the PLSR method. The results from the RF and the KNN methods are similar to Fig. 10 and are included in the Appendix as Figs. 13 and 14. We can observe from the figure that the R^2 for GPP estimation is generally higher than that for SIF estimation at nearly all greenness levels and often by greater amounts at low or high greenness levels. More interestingly, the R^2 varies with greenness level in a similar concave fashion as observed for the linear regression R^2 of GPP versus SIF. The lower R^2 values at low or high greenness in Fig. 10 mean that GPP, SIF, or both have greater portions of their variances attributable to other sources than the five inputs and are thus less predictable, which may explain the lower linear regression R^2 between GPP and SIF at low or high greenness.

4 Discussion

4.1 Uncertainties in Different GPP Estimation Methods

Many methods have emerged for global GPP estimation, and they can be divided into data-based models, LUE models, and process-based models. These models have resulted in a wide range in the estimated global annual sum carbon emission from 112 to 169 Pg C year^{-1},[53,54] indicating uncertainties and variations in the models. These uncertainties are observed in this work. As shown in Fig. 3, the three GPP datasets (FLUXCOM, PML, and VPM) used, which are based on three different estimation methods, differ among areas with different greenness levels.

Remote sensing data, such as surface reflectance, vegetable indices, and various meteorological variables, are used as auxiliary constraints to estimate global GPP, but inconsistent performance among GPP datasets has been observed in studying environmental stresses (such

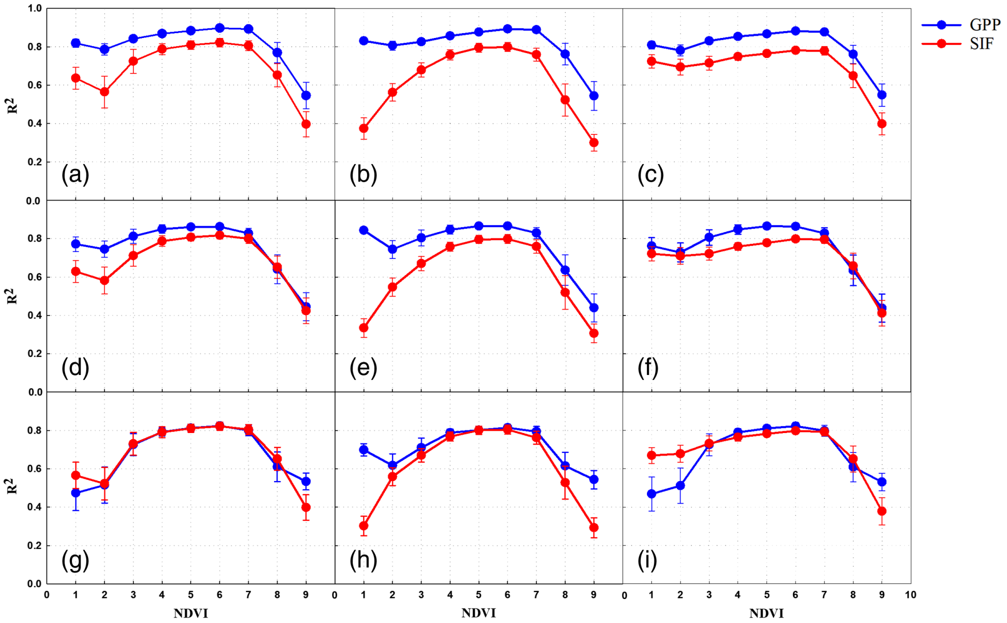

Fig. 10 R^2 values as a function of NDVI for GPP and SIF prediction from SWR, TMP, PRE, VPD, and SM by a PLSR model. (a) FLUXCOM_CSIF; (b) FLUXCOM_SIF005; (c) FLUXCOM_RTSIF; (d) PML_CSIF; (e) PML_SIF005; (f) PML_RTSIF; (g) VPM_CSIF; (h) VPM_SIF005; (i) VPM_RTSIF.

as drought, high temperature), illustrating uncertainties among the GPP estimation models.[55] On a global scale, biases in these auxiliary factors, such as inversion errors in surface reflectance by cloudy climate in rainforest areas,[26,35,56] low signal-to-noise ratios of different remote sensing data in low-productivity ecosystems,[57,58] will lead to uncertainties in GPP estimation in these areas.

Other sources of uncertainty in global GPP estimation include the selection of some vegetation class-specific empirical parameters, such as $\varepsilon_{\max}$ in the LUE models and $V_{c\max}$ in the process-based models. There have been studies specifically addressing these issues.[59,60] The distribution of flux tower sites used for model training in data-based models is also one source of uncertainty. For regions with fewer flux tower sites, the uncertainty of GPP estimations is generally larger.[6] There are fewer tower sites in the tropical rainforest, the Australian SHR region, and the arid region of Central Asia, which can lead to larger errors in GPP estimation as reflected by the lower linear correlations or greater differences among the GPP datasets shown in Fig. 4.

4.2 Robustness of a Linear Relationship Between GPP and SIF

Based on the basic light use efficiency model, $\mathrm{SIF} = \mathrm{APAR} \times \phi_F \times f_{\mathrm{esc}}$ and $\mathrm{GPP} = \mathrm{APAR} \times \mathrm{LUE}$, we can get $\frac{\mathrm{GPP}}{\mathrm{SIF}} = \frac{\mathrm{LUE}}{\phi_F} \frac{1}{f_{\mathrm{esc}}}$ to link and interpret the GPP-SIF relationship, where ϕ_F is the overall light use efficiency for fluorescence emission, LUE is the light use efficiency for photosynthesis, and f_{esc} is the portion of fluorescence detected by sensors.[61] APAR, LUE/ϕ_F, and f_{esc}, as factors in the GPP–SIF relationship, are closely related to vegetation greenness, canopy structure, and environmental factors.[62] The robustness of the GPP–SIF relationship, therefore, varies with location as shown by the regression R^2 in Fig. 5. Further, the global distribution of the slope in Fig. 6 is not a simple function of the greenness level, because it depends on the selected dataset pairs. For areas with relatively high R^2 in Fig. 6, such as areas above 30° N, the slope values are relatively uniform from different dataset pairs, whereas for areas with relatively low R^2, such as Central Asia and the tropical rainforest, the slope tends to be different from different dataset pairs. Low R^2 values thus mean GPP–SIF slope inconsistency and non-robustness. These spatial variations in the linear regression slope for GPP versus SIF (Fig. 6) are consistent with the results of Chen et al.[37] The ratio of GPP/SIF in tropical rain forests and Australian shrublands, however, varies with data sources,[37] which supports the relatively low R^2 of GPP versus SIF in these areas from this work (Fig. 5). The GPP–SIF R^2 for different vegetation classes (Fig. 9) are consistent with the what has been reported for North America.[63]

Figure 7 shows that the R^2 of GPP versus SIF varies with greenness in a concave fashion. In low-greenness areas where NDVI < 0.2, the SIF values are usually less than 0.1 [see Figs. 15(a)–15(c) in Appendix, for examples]. Because of the fragile ecosystems and low signal-to-noise ratios caused by sparse vegetation, the linear relationship between GPP and SIF in these areas is weak.[57,58] In high-greenness areas where NDVI > 0.8, on the other hand, satellite measurements cannot detect all fluorescence activities because of the complexity of the ecosystem and cloudy weather in high productivity areas,[26,35,56] or the lack of variations in GPP and SIF in the steady climate conditions in rainforest areas [see Figs. 15(d)–15(f) in Appendix], the linear relationship between GPP and SIF is also weak. As shown in Fig. 7, the linear relationship between GPP and SIF is the best in mid-greenness areas ($0.3 <$ NDVI < 0.7), where there are more types of plants (Fig. 9) and differences among different types of plants are less influential than in the low- or high- greenness areas. Experiments have shown, for example, that SIF corrected by a site-specific f_{esc} can improve the linear relationship between GPP and SIF, but there is still a lack of a method for the global scale, especially for the comprehensive evaluation of multiple data sources.[64,65] The linear regression R^2 of GPP versus SIF remains a concave function of greenness level for all seasons and dataset pairs (Fig. 8). It can be known that the linear regression R^2 values of GPP versus SIF in MAM and SON were higher than those in JJA and DJF across the NDVI levels. In fact, no matter whether in the north or south hemisphere, plants in MAM or SON (spring or autumn) have moderate photosynthesis intensity, and the coupling relationship between GPP and SIF is more significant. In JJA and DJF, some extreme climates (such as strong light, high temperature, extreme cold) may cause photosynthesis to approach saturation or stop,[66–68] so the changes of SIF and GPP are no longer completely synchronized.

Five environmental variables affecting vegetation photosynthesis predict or explain GPP and SIF to varied degrees, depending on greenness (Fig. 10, and Figs. 13 and 14 in Appendix). The R^2 for GPP or SIF in the mid-greenness areas is greater than that of low- or high-greenness areas. This concave shape resembles and may partially explain the concave shape of the liner regression R^2 of GPP versus SIF because the less predictable/determinable GPP or SIF is, the less definitive the GPP–SIF relationship is likely to be. In addition, GPP and SIF are affected by physiological and non-physiological factors, and the different physiological responses of GPP and SIF to environmental factors will lead to different predicted R^2 for GPP and SIF. GPP is the ultimate product of photosynthesis and may be more sensitive to environmental factors, whereas SIF is mainly an intermediate byproduct of photosystem II,[15] which would cause R^2 for GPP estimation from five environmental variables generally higher than that for SIF estimation at nearly all greenness levels (Fig. 10). However, the detailed explanatory power of environmental factors for GPP and SIF physiology deserves further study. For non-physiological factors, SIF, as an optical signal, can be reflected and reabsorbed in the canopy and then only part of it can be received by sensors (The received portion is represented as f_{esc}), and it is also affected by viewing-illumination geometry,[15,61] which may partly explain that R^2 for GPP estimation is generally higher than that for SIF estimation. To analyze the relationship between GPP and SIF on a global scale, one should, therefore, not only pay attention to the physiological connections between GPP and SIF as influenced by environmental variables but also to low signal-to-noise ratios caused by weak signals in low-greenness areas, complex system structures, and cloudy weather in high-greenness areas. Uncoupling the differential contributions of physical and physiological factors to the GPP–SIF relationship still requires further study.

4.4 Implications From This Study

In this work, we only investigated the spatial distribution of R^2 of a linear relationship between GPP and SIF on the global scale. Nonlinear to linear relationships between GPP and SIF have been extensively studied at the leaf-canopy level, but the biophysical mechanisms behind these relationships on a global scale are still lacking. NPQ is another light energy destination other than photochemistry and chlorophyll fluorescence and its influence on the GPP–SIF relationship at different time scales should also be considered in future work (such as the decoupling of NPQ_r on the diurnal scale and NPQ_s on the seasonal scale). Clearly, more mechanistic process studies are needed to understand the nature of the GPP–SIF relationship. In canopy-global cross-scale analysis, existing studies have shown various linear relationships between GPP and SIF from hourly to monthly scales.[69] Further research, thus, should comprehensively analyze the reliability of the relationship between GPP and SIF at different spatiotemporal scales and identify the key drivers across scales.

In addition to the mechanisms between GPP and SIF on a global scale, accurate retrievals of SIF or GPP, especially in areas with low or high greenness, should be considered as one of the directions to improve the accuracy of GPP estimation based on SIF. For satellite-measured SIF, statistical retrieval algorithms have gradually replaced methods based on the physical processes, which may ignore some complex details in atmospheric corrections. The selection of parameters in the statistical inversion algorithm, such as the reference surface, the fitting window, and the number of principal components (PCs), are still focuses of work to improve the accuracy of the algorithm. In addition, the current retrieval algorithm of red-band SIF is still being studied, which seems to be able to provide a new basis for decoupling the contributions of PSI and PSII to chlorophyll fluorescence. The retrievals of existing satellite SIF data are based on different algorithms and bands, and detector degradation has been detected in satellite sensors.[70] Further research is needed to standardize multi-source SIF satellite data.

5 Conclusion

In this work, we have shown that on a global scale, the robustness of a linear relationship between GPP and SIF follows a concave function of vegetation greenness. The linear relationship is the strongest in the mid-greenness areas, and the linear relationship is much weaker where vegetation greenness is low ($\mathrm{NDVI} < 0.4$) or high ($\mathrm{NDVI} > 0.6$). This study demonstrates the global robustness pattern for estimating GPP based on satellite SIF due to the ability of SIF to track photosynthesis. Low- or high-greenness areas should receive more attention to increase the accuracy of global GPP estimates. Further, the prediction of GPP and SIF from five environmental variables indicates that a lack of determinedness in GPP or SIF in low or high-greenness areas partially explains the weaker linear relationship between GPP and SIF. The results provided useful insights into the robustness of estimating GPP in different areas globally based on multi-satellite measured SIF.

6 Appendix

Figures 11–15 provide additional insights supporting the main findings of this study. Figure 11 presents Seasonal average NDVI from 2001 to 2020. Figure 12 presents Global distribution of eight major vegetation classes in 2015. Figure 13 highlights R^2 values as a function of NDVI for GPP and SIF prediction from SWR, TMP, PRE, VPD, and SM by an RF model, followed by

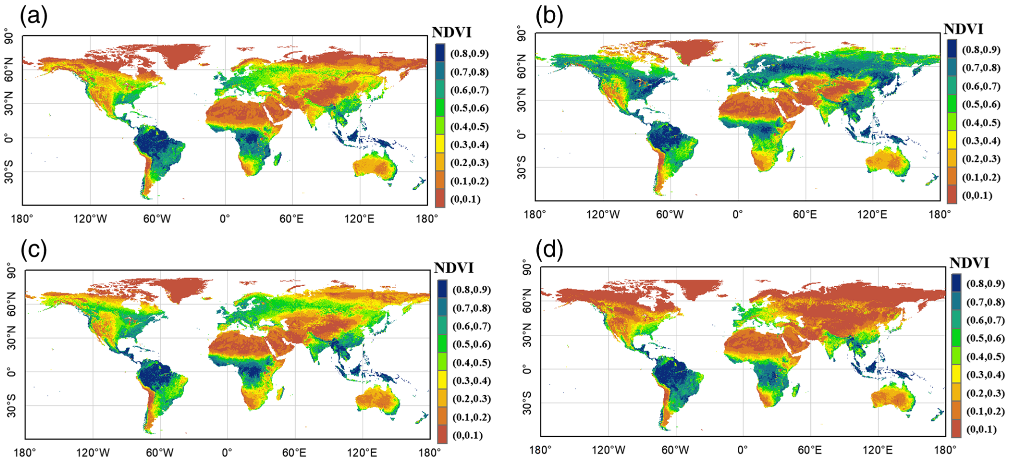

Fig. 11 Seasonal average NDVI from 2001 to 2020. (a) MAM (March to May), (b) JJA (June to August), (c) SON (September to November), and (d) DJF (December to February).

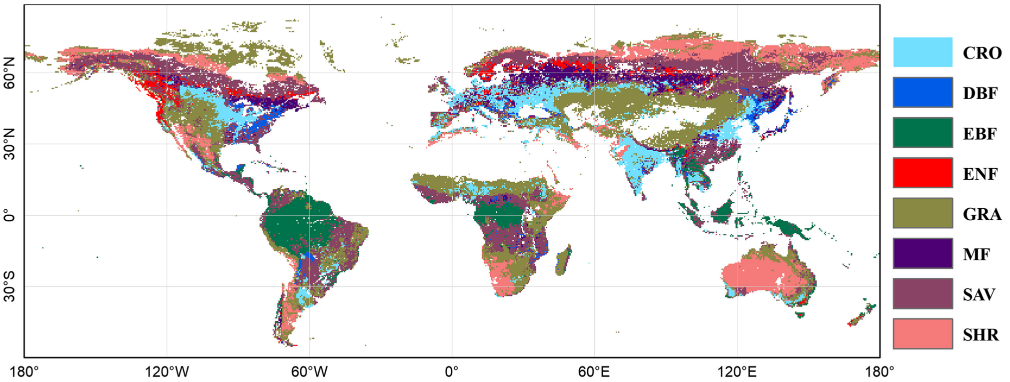

Fig. 12 Global distribution of eight major vegetation classes in 2015. CRO—croplands, DBF—deciduous broadleaf forest, EBF—evergreen broadleaf forest, ENF—evergreen needles forest, GRA—grasslands, MF—mixed forest, SAV—savannas and woody savannas, and SHR—closed shrublands and open shrublands.

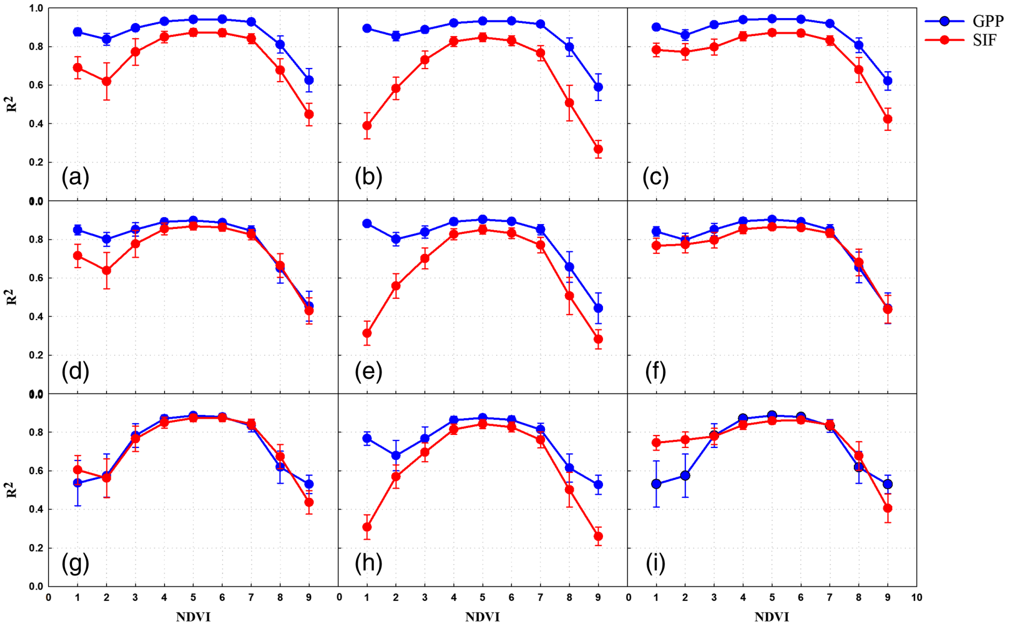

Fig. 13 R^2 values as a function of NDVI for GPP and SIF prediction from SWR, TMP, PRE, VPD, and SM by an RF model. (a) FLUXCOM_CSIF. (b) FLUXCOM_SIF005. (c) FLUXCOM_RTSIF. (d) PML_CSIF. (e) PML_SIF005. (f) PML_RTSIF. (g) VPM_CSIF. (h) VPM_SIF005. (i) VPM_RTSIF.

Fig. 14, which demonstrates R^2 values as a function of NDVI for GPP and SIF prediction from SWR, TMP, PRE, VPD, and SM by a KNN model. Lastly, Fig. 15 summarizes GPP-SIF scatter plots for example locations with low or high greenness.

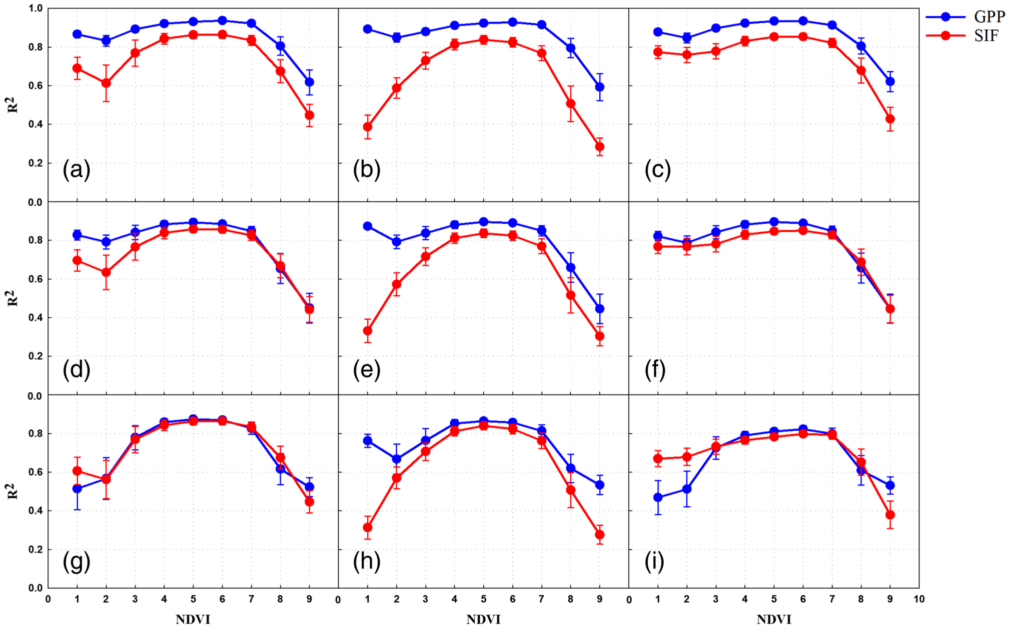

Fig. 14 R^2 values as a function of NDVI for GPP and SIF prediction from SWR, TMP, PRE, VPD, and SM by a KNN model. (a) FLUXCOM_CSIF. (b) FLUXCOM_SIF005. (c) FLUXCOM_RTSIF. (d) PML_CSIF. (e) PML_SIF005. (f) PML_RTSIF. (g) VPM_CSIF. (h) VPM_SIF005. (i) VPM_RTSIF.

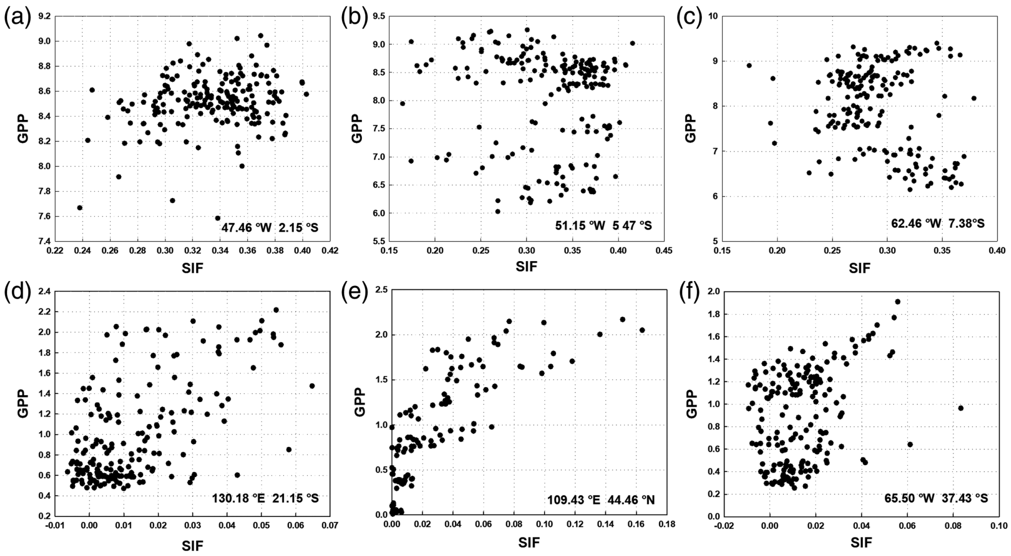

Fig. 15 GPP-SIF scatter plots for example locations with low greenness (a)–(c), NDVI < 0.20 and high greenness (d)–(f), NDVI > 0.8.

Disclosures

The authors have no competing interests to declare.

Code and Data Availability

All data used in this study are public access, which is presented in Sec. 2. All programming and data analysis were done in Python, and related codes can be access from https://github.com/196728abc/Robust.

Acknowledgments

This project is partially supported by the Jiangsu Agricultural Science and Technology Innovation Fund (Grant No. SCX (22)3115), the National Natural Science Foundation of China (Grant Nos. 51961125102 and 31771680), and the 111 Project (Grant No. B23008).

References

1. J. Xiao et al., "Remote sensing of the terrestrial carbon cycle: a review of advances over 50 years," *Remote Sens. Environ.* **233**, 111383 (2019).
2. Y. Y. Pei et al., "Evolution of light use efficiency models: improvement, uncertainties, and implications," *Agric. For. Meteorol.* **317**, 108905 (2022).
3. Y. Chen et al., "Contrasting performance of the remotely-derived GPP products over different climate zones across China," *Remote Sens.* **11**, 1855 (2019).
4. F. Wei et al., "Divergent trends of ecosystem-scale photosynthetic efficiency between arid and humid lands across the globe," *Global Ecol. Biogeogr.* **31**, 1824–1837 (2022).
5. J. Kumar et al., "Understanding the representativeness of FLUXNET for upscaling carbon flux from Eddy covariance measurements," *Earth Syst. Sci. Data Discuss.*, 1–25 (2016).
6. G. Badgley et al., "Terrestrial gross primary production: using NIRv to scale from site to globe," *Glob. Chang. Biol.* **25**, 3731–3740 (2019).
7. G. Tramontana et al., "Predicting carbon dioxide and energy fluxes across global FLUXNET sites with regression algorithms," *Biogeosciences* **13**, 4291–4313 (2016).
8. M. Jung, M. Reichstein, and A. Bondeau, "Towards global empirical upscaling of FLUXNET Eddy covariance observations: validation of a model tree ensemble approach using a biosphere model," *Biogeosciences* **6**, 2001–2013 (2009).
9. S. W. Running et al., "A continuous satellite-derived measure of global terrestrial primary production," *Bioscience* **54**, 547–560 (2004).
10. X. M. Xiao et al., "Satellite-based modeling of gross primary production in an evergreen needleleaf forest," *Remote Sens. Environ.* **89**(4), 519–534 (2004).
11. Y. Q. Zhang et al., "Coupled estimation of 500 m and 8-day resolution global evapotranspiration and gross primary production in 2002–2017," *Remote Sens. Environ.* **222**, 165–182 (2019).
12. C. Jiang and Y. Ryu, "Multi-scale evaluation of global gross primary productivity and evapotranspiration products derived from breathing earth system simulator (BESS)," *Remote Sens. Environ.* **186**, 528–547 (2016).
13. Y. Y. Pei et al., "Performance of four state-of-the-art GPP products (VPM, MOD17, BESS and PML) for grasslands in drought years," *Ecol. Inform.* **56**, 101052 (2020).
14. Y. Zhang et al., "Development of a coupled carbon and water model for estimating global gross primary productivity and evapotranspiration based on eddy flux and remote sensing data," *Agric. For. Meteorol.* **223**, 116–131 (2016).
15. G. H. Mohammed et al., "Remote sensing of solar-induced chlorophyll fluorescence (SIF) in vegetation: 50 years of progress," *Remote Sens. Environ.* **231**, 111177 (2019).
16. J. C. Yang et al., "Gross primary production (GPP) and red solar induced fluorescence (SIF) respond differently to light and seasonal environmental conditions in a subalpine conifer forest," *Agric. For. Meteorol.* **317**, 108904 (2022).
17. J. E. Lee et al., "Forest productivity and water stress in Amazonia: observations from GOSAT chlorophyll fluorescence," *Proc. R. Soc. B* **280**, 20130171 (2013).
18. Y. Zhang et al., "Spatially-explicit monitoring of crop photosynthetic capacity through the use of space-based chlorophyll fluorescence data," *Remote Sens. Environ.* **210**, 362–374 (2018).
19. L. He et al., "Diverse photosynthetic capacity of global ecosystems mapped by satellite chlorophyll fluorescence measurements," *Remote Sens. Environ.* **232**, 111344 (2019).
20. L. Guanter et al., "Global and time-resolved monitoring of crop photosynthesis with chlorophyll fluorescence," *Proc. Natl. Acad. Sci. U. S. A.* **111**(14), E1327–E1333 (2014).
21. Y. Sun et al., "OCO-2 advances photosynthesis observation from space via solar-induced chlorophyll fluorescence," *Science* **358**, eaam5747 (2017).
22. J. Bai et al., "Estimation of global GPP from GOME-2 and OCO-2 SIF by considering the dynamic variations of GPP-SIF relationship," *Agric. For. Meteorol.* **326**, 109180 (2022).
23. X. Yang et al., "Solar-induced chlorophyll fluorescence that correlates with canopy photosynthesis on diurnal and seasonal scales in a temperate deciduous forest," *Geophys. Res. Lett.* **42**, 2977–2987 (2015).
24. Y. Zhang et al., "Model-based analysis of the relationship between sun-induced chlorophyll fluorescence and gross primary production for remote sensing applications," *Remote Sens. Environ.* **187**, 145–155 (2016).
25. J. D. Wood et al., "Multiscale analyses of solar-induced fluorescence and gross primary production," *Geophys. Res. Lett.* **44**, 533–541 (2017).

26. X. Li et al., "Solar-induced chlorophyll fluorescence is strongly correlated with terrestrial photosynthesis for a wide variety of biomes: First global analysis based on OCO-2 and flux tower observations," *Glob. Chang. Biol.* **24**, 3990–4008 (2018).
27. C. Frankenberg et al., "New global observations of the terrestrial carbon cycle from GOSAT: patterns of plant fluorescence with gross primary productivity," *Geophys. Res. Lett.* **38**, L17706 (2011).
28. Y. Zhang et al., "A global spatially contiguous solar-induced fluorescence dataset using neural networks," *Biogeosciences* **15**, 5779–5800 (2018).
29. J. Wen et al., "A framework for harmonizing multiple satellite instruments to generate a long-term global high spatial-resolution solar-induced chlorophyll fluorescence (SIF)," *Remote Sens. Environ.* **239**, 111644 (2020).
30. X. Li and J. Xiao, "A global, 0.05-degree product of solar-induced chlorophyll fluorescence derived from OCO-2, MODIS, and reanalysis data," *Remote Sens.* **11**, 51 (2019).
31. P. Gentine and S. H. Alemohammad, "Reconstructed solar-induced fluorescence: a machine learning vegetation production based on MODIS surface reflectance to produce GOME-2 solar-induced fluorescence," *Geophys. Res. Lett.* **45**, 3136–3146 (2018).
32. X. A. Chen et al., "A long-term reconstructed TROPOMI solar-induced fluorescence dataset using machine learning algorithms," *Sci. Data* **9**, 427 (2022).
33. X. Li and J. Xiao, "Mapping photosynthesis solely from solar-induced chlorophyll fluorescence: a global, fine-resolution dataset of gross primary production derived from OCO-2," *Remote Sens.* **11**(21), 2563 (2019).
34. Y. Chen et al., "Improved global maps of the optimum growth temperature, maximum light use efficiency, and gross primary production for vegetation," *J. Geophys. Res. Biogeosci.* **126**(4), e2020JG005651 (2021).
35. A. Shekhar, N. Buchmann, and M. Gharun, "How well do recently reconstructed solar-induced fluorescence datasets model gross primary productivity?" *Remote Sens. Environ.* **283**, 113282 (2022).
36. T. S. Magney, M. L. Barnes, and X. Yang, "On the covariation of chlorophyll fluorescence and photosynthesis across scales," *Geophys. Res. Lett.* **47**, e2020GL091098 (2020).
37. A. Chen et al., "Moisture availability mediates the relationship between terrestrial gross primary production and solar-induced chlorophyll fluorescence: Insights from global-scale variations," *Glob. Chang. Biol.* **27**, 1144–1156 (2021).
38. S. J. Jeong et al., "Application of satellite solar-induced chlorophyll fluorescence to understanding large-scale variations in vegetation phenology and function over northern high latitude forests," *Remote Sens. Environ.* **190**, 178–187 (2017).
39. J. Bai et al., "The difference between the responses of gross primary production and sun-induced chlorophyll fluorescence to the environment based on tower-based and TROPOMI SIF data," *Appl. Sci.* **14**(2), 771 (2024).
40. M. Jung et al., "Scaling carbon fluxes from eddy covariance sites to globe: Synthesis and evaluation of the FLUXCOM approach," *Biogeosciences* **17**, 1343–1365 (2020).
41. https://www.bgc-jena.mpg.de/geodb/projects/Data.php
42. R. Leuning et al., "A simple surface conductance model to estimate regional evaporation using MODIS leaf area index and the Penman-Monteith equation," *Water Resour. Res.* **44**, W10419 (2008).
43. https://code.earthengine.google.com/?asset=CAS/IGSNRR/PML/V2_v017
44. Y. Zhang et al., "A global moderate resolution dataset of gross primary production of vegetation for 2000–2016," *Sci. Data* **4**, 170165 (2017).
45. https://doi.org/10.6084/m9.figshare.c.3789814.v1
46. https://doi.org/10.6084/m9.figshare.6387494
47. https://cornell.box.com/s/gkp4moy4grvqsus1q5oz7u5lc30i7o41
48. https://doi.org/10.6084/m9.figshare.19336346.v2
49. https://lpdaac.usgs.gov/data/
50. T. R. Loveland and A. S. Belward, "The IGBP-DIS global 1km land cover data set, DISCover: first results," *Int J Remote. Sens.* **18**(15), 3289–3295 (1997).
51. J. T. Abatzoglou et al., "TerraClimate, a high-resolution global dataset of monthly climate and climatic balance from 1958–2015," *Sci. Data* **5**, 170191 (2018).
52. https://code.earthengine.google.com/?asset=IDAHO_EPSCOR/TERRACLIMATE
53. A. Anav et al., "Spatiotemporal patterns of terrestrial gross primary production: a review," *Rev. Geophys.* **53**, 785–818 (2015).
54. Y. Ryu, J. A. Berry, and D. D. Baldocchi, "What is global photosynthesis? History, uncertainties and opportunities," *Remote Sens. Environ.* **223**, 95–114 (2019).
55. L. Zhang et al., "Contrasting the performance of eight satellite-based GPP models in water-limited and temperature-limited grassland ecosystems," *Remote Sens.* **11**, 1333 (2019).
56. H. Tang and R. Dubayah, "Light-driven growth in Amazon evergreen forests explained by seasonal variations of vertical canopy structure," *Proc. Natl. Acad. Sci. U. S. A.* **114**, 2640–2644 (2017).
57. N. Madani et al., "Global analysis of bioclimatic controls on ecosystem productivity using satellite observations of solar-induced chlorophyll fluorescence," *Remote Sens.* **9**, 530 (2017).

58. J. Joiner et al., "New methods for the retrieval of chlorophyll red fluorescence from hyperspectral satellite instruments: simulations and application to GOME-2 and SCIAMACHY," *Atmos. Meas. Tech.* **9**, 3939–3967 (2016).
59. S. Wang et al., "Improving the light use efficiency model for simulating terrestrial vegetation gross primary production by the inclusion of diffuse radiation across ecosystems in China," *Ecol. Complex.* **23**, 1–13 (2015).
60. C. T. de Almeida et al., "Improvements of the MODIS gross primary productivity model based on a comprehensive uncertainty assessment over the Brazilian Amazonia," *ISPRS J. Photogramm. Remote Sens.* **145**, 268–283 (2018).
61. W. Yan et al., "Escape ratio contributes more than fluorescence yield to SIF-GPP relationship over crops and rainforest," *IEEE Geosci. Remote Sens. Lett.* **21**, 1–5 (2024).
62. Z. Zhang et al., "Reduction of structural impacts and distinction of photosynthetic pathways in a global estimation of GPP from space-borne solar-induced chlorophyll fluorescence," *Remote Sens. Environ.* **240**, 111722 (2020).
63. Y. Zhang et al., "Consistency between sun-induced chlorophyll fluorescence and gross primary production of vegetation in North America," *Remote Sens. Environ.* **183**, 154–169 (2016).
64. Z. Zhang et al., "From canopy-leaving to total canopy far-red fluorescence emission for remote sensing of photosynthesis: first results from TROPOMI," *Geophys. Res. Lett.* **46**, 12030–12040 (2019).
65. X. Lu et al., "Comparison of total emitted solar-induced chlorophyll fluorescence (SIF) and top-of-canopy (TOC) SIF in estimating photosynthesis," *Remote Sens. Environ.* **251**, 112083 (2020).
66. G. Wohlfahrt et al., "Sun-induced fluorescence and gross primary productivity during a heat wave," *Sci. Rep.* **8**, 14169 (2018).
67. J. Chen et al., "Effects of low temperature on the relationship between solar-induced chlorophyll fluorescence and gross primary productivity across different plant function types," *Remote Sens.* **14**(15), 3716 (2022).
68. Z. Butterfield et al., "Accounting for changes in radiation improves the ability of SIF to track water stress-induced losses in summer GPP in a temperate deciduous forest," *JGR Biogeosci.* **128**, e2022JG007352 (2023).
69. T. S. Magney et al., "Mechanistic evidence for tracking the seasonality of photosynthesis with solar-induced fluorescence," *Proc. Natl. Acad. Sci. U. S. A.* **116**, 11640–11645 (2019).
70. W. K. Smith et al., "Chlorophyll fluorescence better captures seasonal and interannual gross primary productivity dynamics across dryland ecosystems of southwestern North America," *Geophys. Res. Lett.* **45**, 748–757 (2018).

Lijiang Fu is a PhD student at the Key Laboratory of Advanced Process Control for Light Industry at Jiangnan University, China. His research focuses on vegetation remote sensing, ecosystem carbon assessment, and vegetation drought detection.

Qian Xia received her PhD from Jiangnan University in 2023. She is a lecturer at Changshu Institute of Technology, China. Her research focuses on plant chlorophyll fluorescence analysis, plant drought detection, and deep learning.

Hao Tang is a PhD student at the Key Laboratory of Advanced Process Control for Light Industry at Jiangnan University, China. His research focuses on chlorophyll fluorescence equipment development, signal processing, and detection.

Junqing Chen is a PhD student in the Department of Chemical and Biomedical Engineering at the University of Missouri-Columbia, United States. Her research focuses on plant photosynthesis modeling and parameter identification.

Jinglu Tan received his PhD from the University of Minnesota, United States, in 1990. He is a James C. Dowell Professor at the University of Missouri-Columbia, United States. His research focuses on modeling and sensing of photoelectron transduction in plants, modeling and kinetic analysis of energy metabolism in muscles, modeling of oxygen transport in cardiopulmonary systems, and ultrasound sensing and measurement of rheological properties.

Ya Guo received his PhD from the University of Missouri-Columbia, United States, in 2009. He is a professor at Jiangnan University, China. His research focuses on Instrument development, optical detection, and vegetation remote sensing.